

RESEARCH ARTICLE

A novel adaptive class weight adjustment-based multiclass segmentation error minimization technique for COVID-19 X-ray image analysis

Leena Samantaray¹ | Rutuparna Panda²  | Manoj Kumar Naik³ |
Ajith Abraham⁴

¹Department of Electronics and Communication Engineering, Ajay Binay Institute of Technology, Cuttack, India

²Department of Electronics and Telecommunication Engineering, Veer Surendra Sai University of Technology, Burla, India

³Faculty of Engineering and Technology, Siksha O Anusandhan, Bhubaneswar, India

⁴FLAME University, Washington, Pune, India

Correspondence

Rutuparna Panda, Department of Electronics and Telecommunication Engineering, Veer Surendra Sai University of Technology, Burla, Odisha 768018, India.

Email: rpanda_etc@vssut.ac.in

Manoj Kumar Naik, Faculty of Engineering and Technology, Siksha O Anusandhan, Bhubaneswar, Odisha 751030, India.

Email: manojnaik@soauniversity.ac.in

Abstract

Coronavirus outbreaks during the last couple of years created a huge health disaster for human lives. Diagnosis of COVID-19 infections is, thus, very important for the medical practitioners. For a quick detection, analysis of the COVID-19 chest X-ray images is inevitable. Therefore, there is a strong need for the development of a multiclass segmentation method for the purpose. Earlier techniques used for multiclass segmentation of images are mostly based on entropy measurements. Nonetheless, entropy methods are not efficient when the gray-level distribution of the image is nonuniform. To address this problem, a novel adaptive class weight adjustment-based multiclass segmentation error minimization technique for COVID-19 chest X-ray image analysis is investigated. Theoretical investigations on the first-hand objective functions are presented. The results on both the biclass and multiclass segmentation of medical images are enlightened. The key to our success is the adjustment of the pixel counts of different classes adaptively to reduce the error of segmentation. The COVID-19 chest X-ray images are taken from the Kaggle Radiography database for the experiments. The proposed method is compared with the state-of-the-art methods based on Tsallis, Kapur's, Masi, and Rényi entropy. The well-known segmentation metrics are used for an empirical analysis. Our method achieved a performance increase of around 8.03% in the case of PSNR values, 3.01% for FSIM, and 4.16% for SSIM. The proposed technique would be useful for extracting dots from micro-array images of DNA sequences and multiclass segmentation of the biomedical images such as MRI, CT, and PET.

KEYWORDS

biomedical image processing, COVID-19 X-ray image analysis, multiclass segmentation, radiology

1 | INTRODUCTION

The World Health Organization (WHO) declared the epidemic of the COVID-19 infection as a pandemic. The

cause of the illness is SARS-CoV-2 (severe acute respiratory syndrome 2). Combating against the spread of coronavirus (COVID-19) infection is an important task in today's era. Therefore, there is a strong need for the early

detection followed by an analysis to interpret the severity of the infection. For detection, various methods used are—the antigen test, reverse transcription-polymerase chain reaction (RT-PCR), and serology testing.¹ For interpretation of the severity of the disease, chest X-ray images from patients are used by the radiologists.^{2,3} Moreover, the false-negative report of the RT-PCR test² warrants further analysis by using the chest X-ray images. Other imaging techniques used by the radiologists are CT, MRI, PET, etc. However, chest X-ray images are mostly preferred because these are easily available with low cost. Commonly used for the analysis and interpretation, even though X-ray images offer a lower sensitivity.

Multiclass segmentation is popular to divide the X-ray image into different regions. The partitioning of the image under consideration is crucial. The accuracy of segmentation depends on the method used. Many recent studies^{4–10} described different entropy-based methods together with the machine intelligence for multiclass segmentation of COVID-19 X-ray images. Liu et al.⁴ presented a multilevel COVID 19 X-ray image segmentation technique by maximizing Kapur's entropy objective function. They claimed that Kapur's entropy is easy for computation. Similarly, Kapur's entropy-based multiclass segmentation method for COVID 19 X-ray images was also presented in Reference [5] Sharma et al.⁶ discussed Tsallis entropy-based multilevel thresholding method for image segmentation. These authors claimed that Tsallis entropy-based method yielded better results than Kapur's entropy-based technique. Su et al.⁷ have also used Kapur's entropy together with the multiverse optimization for analysis of COVID-19 X-ray images. Murillo-Olmos et al.⁸ also used Kapur's entropy for multilevel thresholding of COVID-19 X-ray images. The reason of the choice of using Kapur's entropy may be due to the simplicity in implementation. The authors in Reference [9] presented Kapur's entropy-based fitness function for COVID-19 X-ray image segmentation.

The authors in Reference [10] have used the beta differential evolution approach for maximizing Kapur's entropy. They have presented interesting results on multilevel segmentation of color images. Masi entropy was introduced in Reference [11] The authors in Reference [12] suggested practical Masi entropy-based multiclass segmentation of images. Rényi's entropy fitness function is used in Reference [13] for multilevel image segmentation. A detail survey on image thresholding methods is presented in Reference [14] Tsallis entropy-based optimal multiclass segmentation was presented in Reference [15] The authors in References [16–19] used Kapur's entropy for multilevel threshold selection using an optimization algorithm. Sarkar and das²⁰ have used 2D Tsallis

entropy-based fitness function for multiclass segmentation of images. They have claimed regarding the preservation of the contextual information. Rényi entropy-based image thresholding technique was presented by Sarkar et al.²¹ However, these entropy-based methods yield inaccurate results due to their dependency on the image histograms. Nonetheless, 1D, 2D, or 3D image histograms are used to compute the entropic values. Usually, the gray-level spatial distributions are nonuniform in these histograms.

This is the motivation behind our investigations. New theoretical results are introduced in this work. The first-hand objective functions are investigated. These functions are minimized by using an optimizer called opposition equilibrium optimizer OEO.^{22,23} The proposal is first validated on two-class segmentation by extracting dots from micro-array images of DNA sequences.^{24,25} Recently, the X-ray image analysis is found as a worthwhile subject of study.^{26,27} In this context, the multiclass segmentation techniques may be very useful. In this paper, the suggested methodology is also used for multiclass segmentation of COVID-19 chest X-ray images. Experiments are carried out considering COVID-19 chest X-ray images from the Kaggle database.²⁸ There is a need for implementation of the administrative, physical, and technical safeguards for the software platform handling patient health information. Recently, Sanghvi et al.²⁹ suggested a model using deep learning (DenseNet201) to analyze the Chest X-ray images of COVID-19-affected patients with the Health Insurance Portability and Accountability Act (HIPAA) compliance. Parmar et al.³⁰ presented a comprehensive study on secured password-less authentication protocol for mobile e-health system.

The rest of the paper is organized as follows. Section 2 describes the preliminary ideas on entropy-based techniques. The proposed method is discussed in Section 3. The results and discussions are presented in Section 4. The concluding remark is given in Section 5.

2 | MATERIALS AND METHODS

2.1 | Tsallis entropy-based method

Tsallis nonextensive entropy-based technique used for multiclass segmentation⁶ is discussed in this section. Let us assume that there are L numbers of gray levels in the image under consideration. Also, it is assumed that the range of these gray levels is $\{1, 2, \dots, L\}$. Note that the probability distributions are $p_i = p_1, p_2, \dots, p_L$. The probability distributions for two classes, class A and class B , are derived as:

$$p_A = \frac{p_1}{p^A}, \frac{p_2}{p^A}, \dots, \frac{p_T}{p^A} \text{ and } p_B = \frac{p_{T+1}}{p^B}, \frac{p_{T+2}}{p^B}, \dots, \frac{p_L}{p^B} \quad (1)$$

where,

$$p^A = \sum_{i=1}^T p_i \text{ and } p^B = \sum_{i=T+1}^L p_i \quad (2)$$

The optimum value of the threshold for two class segmentation is given by:

$$T^* = \arg \max [S_q^A(T) + S_q^B(T) + (1-q) \cdot S_q^A(T) \cdot S_q^B(T)] \quad (3)$$

where q is the Tsallis parameter, $S_q^A(T)$ and $S_q^B(T)$ are estimated as:

$$S_q^A(T) = \frac{1 - \sum_{i=1}^T \left(\frac{p_i}{p^A}\right)^q}{q-1} \text{ and } S_q^B(T) = \frac{1 - \sum_{i=T+1}^L \left(\frac{p_i}{p^B}\right)^q}{q-1} \quad (4)$$

The actual idea is to maximize the information measure between the two classes (object and background). The corresponding gray value needed to maximize the objective functions is coined as the optimum threshold. The idea is then extended to the multiclass segmentation.

The optimum threshold selection criterion for solving a multiclass segmentation problem is given by:

$$[T_1^*, T_2^*, T_3^*, \dots, T_K^*] = \arg \max \left[\frac{S_q^A(T) + S_q^B(T) + \dots + S_q^K(T) + (1-q) \cdot S_q^A(T) \cdot S_q^B(T) \cdot \dots \cdot S_q^K(T)}{S_q^A(T) \cdot S_q^B(T) \cdot \dots \cdot S_q^K(T)} \right] \quad (5)$$

where,

$$\begin{aligned} S_q^A(T) &= \frac{1 - \sum_{i=1}^{T_1} \left(\frac{p_i}{p^1}\right)^q}{q-1}, \\ S_q^B(T) &= \frac{1 - \sum_{i=T_1+1}^{T_2} \left(\frac{p_i}{p^2}\right)^q}{q-1} \text{ and} \\ S_q^K(T) &= \frac{1 - \sum_{i=T_{K-1}+1}^L \left(\frac{p_i}{p^K}\right)^q}{q-1}. \end{aligned}$$

The above objective function (5) is used for solving the problem of the multiclass segmentation.

2.2 | Kapur's entropy-based technique

The Kapur's entropy function is used for multiclass segmentation in References [7–9] This method is totally

dependent on the spatial domain distribution of the gray levels. The scheme uses the histogram. The technique is often used to compute the optimal thresholds by maximizing the total entropy. For a two-class image segmentation, the objective function is given as:

$$T^* = \arg \max (H_A + H_B) \quad (6)$$

where, H_A and H_B are two different entropy values, which are computed by:

$$H_A = \sum_{i=1}^T \frac{p_i}{p^A} \ln \left(\frac{p_i}{p^A} \right), \text{ and } H_B = \sum_{i=T+1}^L \frac{p_i}{p^B} \ln \left(\frac{p_i}{p^B} \right) \quad (7)$$

Note that, p_i , p^A , and p^B are the probability distribution of the gray values, class probability of A and B , respectively, described in Equation (1) and Equation (2). The idea is then extended to the multiclass segmentation. The image is partitioned into $K+1$ classes. Note that the K number of thresholds are used for the partition. For the multiclass segmentation, Kapur's function is written as:

$$[T_1^*, T_2^*, T_3^*, \dots, T_K^*] = \arg \max \left(\sum_{k=1}^K H_k \right) \quad (8)$$

Here, $T = [T_1, T_2, \dots, T_K]$. Note that there are K numbers of thresholds and $K+1$ numbers of classes. For a gray-scale image, we need to compute K optimum thresholds. This is a maximization problem. The entropy values are computed separately as:

$$\begin{aligned} H_1 &= \sum_{i=1}^{T_1} \frac{p_i}{p^1} \ln \left(\frac{p_i}{p^1} \right), H_A = \sum_{i=T_1+1}^{T_2} \frac{p_i}{p^2} \ln \left(\frac{p_i}{p^2} \right), \dots, \\ H_K &= \sum_{i=T_{K-1}+1}^L \frac{p_i}{p^K} \ln \left(\frac{p_i}{p^K} \right) \end{aligned} \quad (9)$$

2.3 | Masi entropy-based method

The Masi entropy is used for multiclass image segmentation in References [11,12] The inherent property of the Masi entropy is that it can deal with the additive/non-extensive information. Assume that I is the image with the dimension $M \times N$. There are L number of gray levels. The range of these levels is $[0, L-1]$. Note that the probability of each gray level is:

$$p_i = \frac{n_i}{M \times N}, i \in [0, 1, \dots, L-1] \quad (10)$$

Interestingly,

$$\sum_{i=0}^{L-1} p_i = 1, \text{ where } p_i > 0 \quad (11)$$

For the two-class segmentation, foreground (C_f) and background (C_b), it is needed to separate both the classes by selecting a threshold $T \in [1, 2, \dots, L-2]$. The foreground class probability (ω_f) is given as:

$$\omega_f = \sum_{i=1}^T p_i, \quad (12)$$

and the background class probability (ω_b) is given by:

$$\omega_b = \sum_{i=T+1}^L p_i. \quad (13)$$

The foreground class Masi entropy (H_f) is calculated as

$$H_f = \frac{1}{1-r} \log \left[1 - (1-r) \sum_{i=1}^T \left(\frac{p_i}{\omega_f} \right) \log \left(\frac{p_i}{\omega_f} \right) \right], \quad (14)$$

and the background class Masi entropy (H_b) is computed as:

$$H_b = \frac{1}{1-r} \log \left[1 - (1-r) \sum_{i=T+1}^L \left(\frac{p_i}{\omega_b} \right) \log \left(\frac{p_i}{\omega_b} \right) \right] \quad (15)$$

where r is the entropy parameter, which is chosen as 0.5.

The two-class segmentation using Masi entropy is described by:

$$H_{(T)} = H_f + H_b, \quad (16)$$

and the optimal threshold T^* is computed as:

$$T^* = \arg \max_{0 < T < L-1} (H_{(T)}). \quad (17)$$

The authors in Reference [12] extended the idea to multiclass segmentation. The number of thresholds is greater than 1. The image is partitioned into $K+1$ classes, i.e., $= \{C_0, C_1, \dots, C_{K-1}, C_K\}$. Here, K threshold

values T_1, T_2, \dots, T_K are used. The intensity values of dissimilar classes are assigned to:

$$\begin{aligned} [0, T_1 - 1] &\in C_0 \\ [T_1, T_2 - 1] &\in C_1 \\ &\dots \\ [T_K, L - 1] &\in C_K \end{aligned} \quad (18)$$

where $0 < T_1 < T_2 < \dots < T_K < L - 1$.

The various class probabilities are given as:

$$\omega_0 = \sum_{i=1}^{T_1} p_i, \omega_1 = \sum_{i=T_1+1}^{T_2} p_i, \dots, \omega_K = \sum_{i=T_K+1}^L p_i. \quad (19)$$

The Masi entropy H_j for the i th class is computed by:

$$H_j = \frac{1}{1-r} \log \left[1 - (1-r) \sum_{i=T_j+1}^{T_{j+1}} \left(\frac{p_i}{\omega_j} \right) \log \left(\frac{p_i}{\omega_j} \right) \right], \quad (20)$$

where $0 \leq j \leq K$.

Thus, the multiclass segmentation problem using Masi entropy is described as:

$$H_{(T_1, T_2, \dots, T_K)} = H_0 + H_1 + \dots + H_K \quad (21)$$

The optimal thresholds $\{T_1^*, T_2^*, \dots, T_K^*\}$ using Masi entropy is defined below:

$$\{T_1^*, T_2^*, \dots, T_K^*\} = \arg \max_{0 < T_1 < T_2 < \dots < T_K < L-1} (H_{(T_1, T_2, \dots, T_K)}). \quad (22)$$

Note that Equation (22) is used for solving the multiclass segmentation problems.

2.4 | Rényi Entropy-based technique

Rényi entropy¹³ with order α is defined as given below:

$$H_\alpha(X) = \frac{1}{(1-\alpha)} \log \left(\sum_{i=1}^n p_i^\alpha \right) \quad (23)$$

Note that X is a discrete random variable, n is an integer, p_i is the i -th probability.

And $0 \leq \alpha \leq \infty$. Basically, Rényi entropy is a more generalization to the Shannon type.

For a two-level segmentation, we consider only two classes. i.e., the foreground (C_f) and the background (C_b). This partition is separated by a threshold

$T \in [1, 2, \dots, L-2]$. Then the foreground class probability (ω_f) is given as:

$$\omega_f = \sum_{i=1}^T p_i, \quad (24)$$

and the background class probability (ω_b) is given by:

$$\omega_b = \sum_{i=T+1}^L p_i. \quad (25)$$

The foreground class Rényi entropy (H_f) is computed as:

$$H_f = \frac{1}{1-\alpha} \log \sum_{i=1}^T \left(\frac{p_i}{\omega_f} \right)^\alpha \quad (26)$$

and the background class Rényi entropy (H_b) is calculated as:

$$H_b = \frac{1}{1-\alpha} \log \sum_{i=T+1}^L \left(\frac{p_i}{\omega_b} \right)^\alpha \quad (27)$$

The two-class segmentation using the Rényi entropy is described by:

$$H_{(T)} = H_f + H_b \quad (28)$$

The optimal threshold T^* based on Rényi entropy can be defined as

$$T^* = \arg \max_{0 < T < L-1} (H_{(T)}) \quad (29)$$

The authors in Reference [13] extended the idea to multiclass segmentation. In this case, the number of thresholds is more than 1. Here, the image is partitioned into $K+1$ classes, that is, $C = \{C_0, C_1, \dots, C_{K-1}, C_K\}$. The foreground class is denoted as C_0 , the intermediate classes are represented as $C_{i=1,2,\dots,K-1}$, and the background class is C_K . It is important to note here that K thresholds T_1, T_2, \dots, T_K are used to generate these classes. The gray-level assignments are shown below:

$$\begin{aligned} [0, T_1 - 1] &\in C_0 \\ [T_1, T_2 - 1] &\in C_1 \\ &\dots \\ [T_K, L - 1] &\in C_K \end{aligned} \quad (30)$$

It may be noted that $0 < T_1 < T_2 < \dots < T_K < L-1$. The various class probabilities are:

$$\omega_0 = \sum_{i=1}^{T_1} p_i, \omega_1 = \sum_{i=T_1+1}^{T_2} p_i, \dots, \omega_K = \sum_{i=T_K+1}^L p_i \quad (31)$$

Then, the Rényi entropy H_j for the i th class is compute by:

$$H_j = \frac{1}{1-\alpha} \log \sum_{i=T_j+1}^{T_{j+1}} \left(\frac{p_i}{\omega_j} \right)^\alpha, \text{ where } 0 \leq j \leq K \quad (32)$$

The multiclass segmentation using the Rényi entropy is described as:

$$H_{(T_1, T_2, \dots, T_K)} = H_0 + H_1 + \dots + H_K \quad (33)$$

The optimal thresholds $\{T_1^*, T_2^*, \dots, T_K^*\}$ using the Rényi entropy are obtained as:

$$\{T_1^*, T_2^*, \dots, T_K^*\} = \arg \max_{0 < T_1 < T_2 < \dots < T_K < L-1} (H_{(T_1, T_2, \dots, T_K)}) \quad (34)$$

It may be noted that Equation (34) is used for solving the multiclass segmentation problems.

3 | THE PROPOSED METHOD

In this section, a novel objective function is proposed. The class weights are adaptively adjusted to compute the optimal thresholds for multiclass segmentation. The idea is to minimize the error in the segmented outputs. The scheme is shown in Figure 1. The optimizer OEO is used for minimizing the suggested objective (fitness) function. The number of segmented classes is predefined. The optimal threshold values are obtained by minimizing the segmentation error (maximizing the pixel counts of classes). Finally, the segmented output is constructed using the image reconstruction rules as discussed below.

Let I be the image of size $M \times N$. The pixel intensity range is $[0, L-1]$. Let us first solve the problem for the two-class segmentation of I as $R \in \{0, 1\}^{M \times N}$. Let us assume any gray value for the threshold T from the range of values $1 < T < (L-1)$. This value of T is used to divide the image I into the two distinct classes, i.e., C_0 and C_1 . The partitioned image is shown as:

$$I_T^s = \begin{cases} C_0 & 0 \leq I_i < T \\ C_1 & T \leq I_i < L-1 \end{cases} \quad (35)$$

Note that I_i denotes the intensity of the i -th pixel and $L = 256$. The error of the two-class segmented output (image I_T^s with $s = 2$) is defined below:

$$error_{(T)} = \sum_{i=1}^T \left(\frac{I_i - \mu_{C_0}}{L} \right)^2 + \sum_{i=T+1}^L \left(\frac{I_i - \mu_{C_1}}{L} \right)^2 \quad (36)$$

Let S be the total number of pixels in an image, equal to $M \times N$. Interestingly, it is implicit in Equation (36) that the error depends on the value of the threshold (T). Therefore, the error is reduced iteratively changing the class weights. The value of T , for which the error is minimum, is called the optimal threshold. It is achieved using the optimum class weights (N_{C_0} and N_{C_1}) adaptively for two different classes C_0 and C_1 . These class weights play the central role in this method. The focus here is to simply adjust the pixel counts (N_{C_0} and N_{C_1}) to reduce the error of segmentation. These counts are either maximized or minimized by using an optimizer, even though an exhaustive search strategy would solve the problem. The reason is that the time requirement is more in the case of an exhaustive search.

The mean value of the class C_0 is defined by:

$$\mu_{C_0}(T) = \frac{\sum_{i=1}^T I_i}{N_{C_0}} \quad (37)$$

and the mean value of the class C_1 is defined as:

$$\mu_{C_1}(T) = \frac{\sum_{i=T+1}^L I_i}{N_{C_1}} \quad (38)$$

where N_{C_0} and N_{C_1} denote the total number of pixels in the classes C_0 and C_1 , respectively. It is reiterated that $N_{C_0} + N_{C_1} = S$. Where, S is the total pixel count, N_{C_0} and N_{C_1} are individual pixel counts. These counts are optimized to minimize the error. The corresponding T is the required threshold. Thus, the objective function for the two-class segmentation is defined as:

$$error_{(T^*)} = \arg \min_{0 < T < L-1} error_{(T)} \quad (39)$$

where T^* represents the optimal threshold.

The idea is extended here for the multiclass segmentation. For a multiclass segmentation, K numbers of the optimal thresholds are required. These thresholds are used to divide the image I into a partitioned image $I_{(T_1, T_2, \dots, T_K)}^s$ (with $s = K + 1$). The partitioned image $I_{(T_1, T_2, \dots, T_K)}^q$ has the $K + 1$ number of classes, i.e., $C_0, C_1, \dots, C_K, C_{K+1}$. It is described by:

$$I_{(T_1, T_2, \dots, T_K)}^s = \begin{cases} C_0 & 0 \leq I_i < T_1 \\ C_1 & T_1 \leq I_i < T_2 \\ \vdots & \vdots \\ C_{K+1} & T_K \leq I_i < L-1 \end{cases} \quad (40)$$

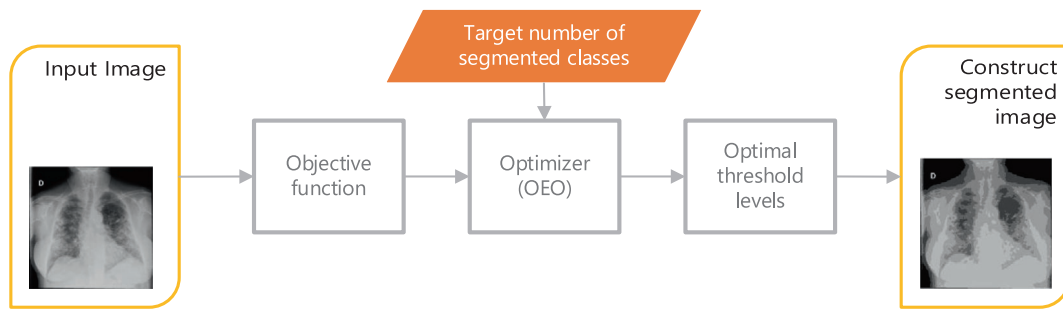


FIGURE 1 Proposed method.

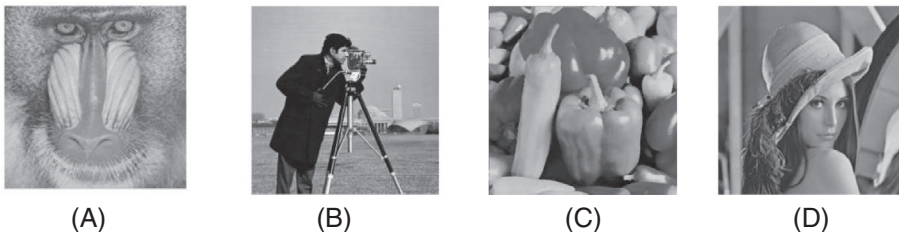


FIGURE 2 Four standard test images. (A) Baboon, (B) Man, (C) Pepper, (D) Lena.

The error for the multiclass segmentation is defined as:

$$\begin{aligned} error_{(T_1, T_2, \dots, T_K)} = & \sum_{i=1}^{T_1} \left(\frac{I_i - \mu_{C_0}}{L} \right)^2 \\ & + \sum_{i=T_1+1}^{T_2} \left(\frac{I_i - \mu_{C_1}}{L} \right)^2 + \dots \\ & + \sum_{i=T_{K+1}}^L \left(\frac{I_i - \mu_{C_{K+1}}}{L} \right)^2 \end{aligned} \quad (41)$$

The mean value of the k th class is defined as:

$$\mu_{C_k}(T_1, T_2, \dots, T_K) = \frac{\sum_{i=T_{k+1}}^{T_{k+1}-1} I_i}{N_{C_k}} \quad (42)$$

The condition is that $0 < T_1 < T_2 < \dots < T_K < (L-1)$ and $\sum_{k=0}^K N_{C_k} = S$.

Need to mention here that $(T_1^*, T_2^*, \dots, T_K^*)$ are the optimal thresholds obtained by minimizing the following objective function:

$$error_{(T_1^*, T_2^*, \dots, T_K^*)} = \arg \min_{0 < T_1 < T_2 < \dots < T_K < (L-1)} error_{(T_1, T_2, \dots, T_K)} \quad (43)$$

TABLE 1 Time required computing the optimal threshold(s).

	<i>Time_{two-class}</i> (sec)	<i>Time_{three-class}</i> (sec)
Baboon	0.3401	86.2507
Man	0.3011	78.6051
Peppers	0.3305	84.1464
Lena	0.3230	82.4341

The optimal thresholds $T_1^*, T_2^*, \dots, T_K^*$ are obtained using the fitness function Equation (43). This is a minimization problem. It is expected to achieve good results,

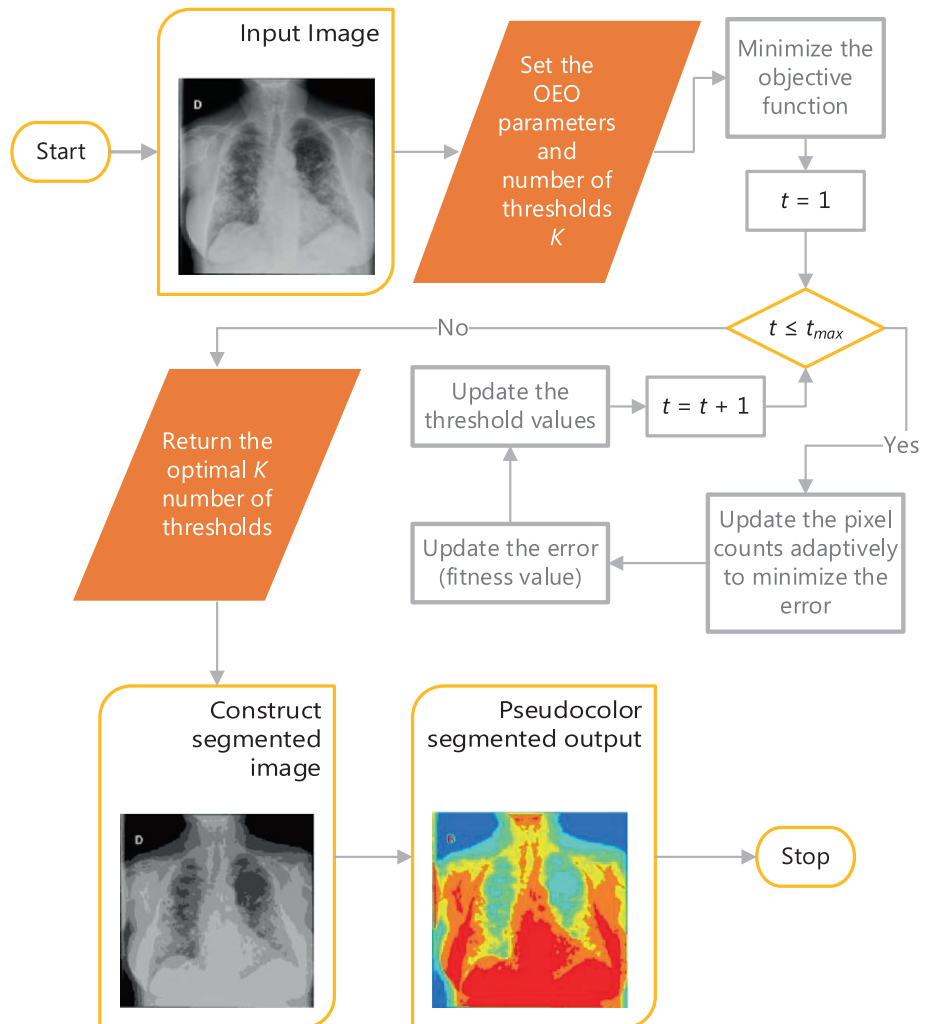


FIGURE 3 Flowchart of the suggested method.

because the error in the multiclass segmentation procedure is minimized through the adjustment of the class weights adaptively. It is noteworthy to mention here that the proposed method needs not to be initialized with a fixed class weight. The initial class weights are chosen randomly within the range $[2, L-2]$. In addition, the scheme is free from the distribution of the gray-level values in the image histogram. Here, we need to optimize the pixel counts N_{C_k} only in the different segmented classes, as opposed to other techniques based on the image histogram (entropy-based). Therefore, the method is the simplest one while considering the implementation.

For a better illustration, four standard test images, namely the Baboon, Man, Peppers, and Lena with size

256×256 , are considered. These images are displayed in Figure 2.

The time complexity of the proposed method is empirically illustrated in Table 1. The time taken in seconds to compute the optimal threshold value(s) for two-class and three-class segmentation is displayed in Table 1. Note that the suggested fitness function Equation (43) is used here for the computation of the optimal threshold(s). This is the execution time complexity of our method while considering the exhaustive search. It may be noted that the MATLAB R2018b is used for the implementation. The Intel Core i3 (5th generation) processor is used for processing. This is evident from the time complexity values that the computation time increases for increasing number of thresholds. The order of the computational complexity for K numbers of thresholds is $O(L^K)$.

From the empirical findings (see Table 1), it is described by the relation $time_{three-class} \approx L \times time_{two-class}$. It is noteworthy to mention here that we need two ($K=2$) numbers of thresholds for three-class segmentation. Therefore, the order of the computational time complexity for three-class segmentation is $O(L^2)$, whereas for two-class segmentation is $O(L)$. This is empirically proved through the exhaustive search process. Need to mention here that the computation time increases exponentially with an increase in the threshold number. Hence, when we talk about the multiclass segmentation, there is a strong need to reduce the time complexity. Obtaining the optimal thresholds through an exhaustive search for multiclass segmentation is quite difficult. To reduce the computational burden, an efficient optimizer is recommended. A flow chart for the proposed method is shown in Figure 3.

4 | RESULTS AND DISCUSSION

In this work, the method is implemented using the MATLAB R2018b. The Intel Core i3 (5th generation) processor is used for both the experiments. The opposition equilibrium optimization (OEO)^{22,23} algorithm is used for

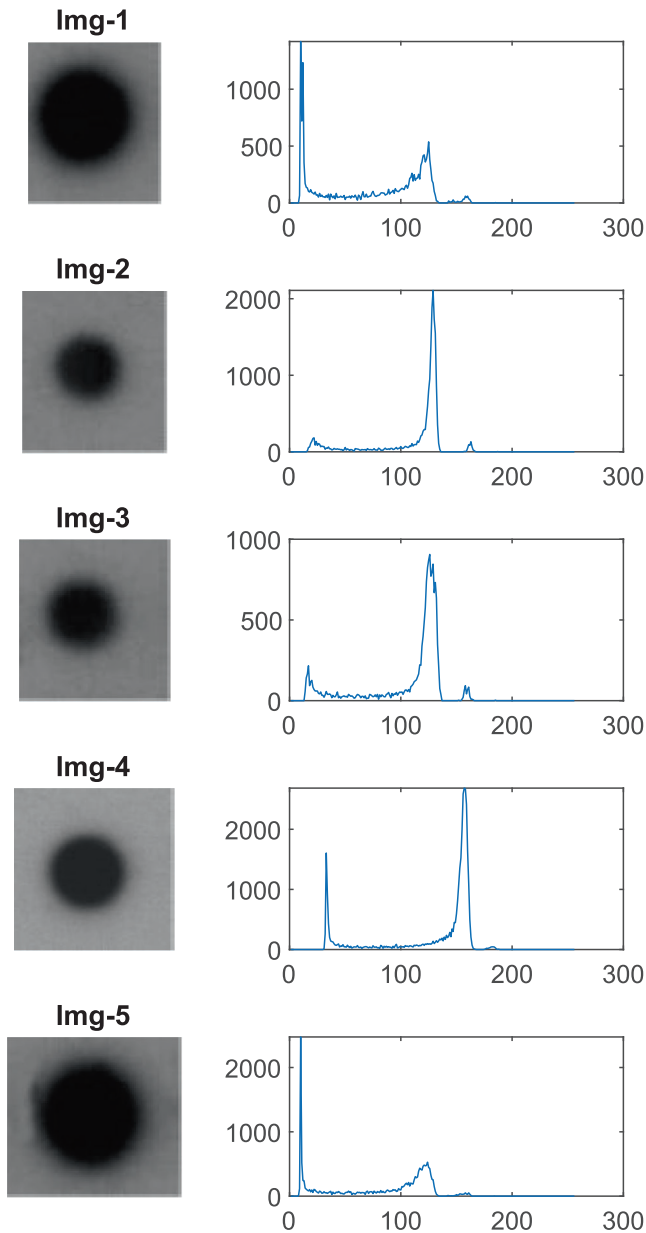


FIGURE 4 Sample test images and their respective histograms.

TABLE 2 Threshold (T) value obtained for two-class segmentation using various methods.

Image	Proposed	Tsallis	Kapur's	Masi	Rényi
Img-1	66	80	89	92	80
Img-2	81	82	102	105	82
Img-3	79	80	100	102	81
Img-4	98	105	133	137	106
Img-5	67	81	96	100	80

minimizing the objective function proposed above. The OEO parameters are taken same as in References [22,23]. Note that the test image bit length of each pixel is 8-bit (with 256 gray levels). In these experiments, we reduce the number of gray levels (for output segmented images) to $K + 1$ with K threshold values. However, the pixel length is still 8-bit.

4.1 | Experiment 1

In this section, the results on two-class segmentation using our method are presented. In practice, two-class and multiclass segmentation methods have their own application advantages, although the primary focus of this work is the multiclass segmentation. Here, the fundamental idea of the two-class segmentation is highlighted through exemplary experiments. It is noteworthy to mention here that a method needs to perform well for the two-class segmentation first. It requires validation. Therefore, we have considered the validation of our method for the use in Bioinformatics analysis and data interpretation. Its performances are compared with the existing entropy-based techniques.

Recently research is concentrated on the next-generation sequencing (NGS) used for DNA variant/mutation detection.²⁴ This, in turn, helps medical practitioners for disease diagnosis, prognosis, therapeutic decision, and follow-up action. Extraction of dots from the background of the gene images of micro-arrays^{24,25} is a

critical task. Nonetheless, these dots have diffused boundaries. Therefore, to achieve good results, it is necessary to make the method free from the gray level distribution. The following results with an in-depth analysis may create interest among the readers.

Five different sample images (Img-1, Img-2, Img-3, Img-4, and Img-5), taken in this experiment, are displayed in Figure 4. Their corresponding histograms with two intensity classes are also shown in the right-hand side. Sometimes, the background intensity class is found dominant over the object. For instance, the background class is dominant over the object displayed in Img-4 (see the corresponding image histogram with a dominant peak on the higher side of the gray levels). In Img-5, the object is dominant over the background (see the corresponding image histogram with a dominant peak on the lower side of the gray levels). Moreover, at the boundary, the dots are diffused. Therefore, it is crucial to find a fair threshold value to detect the intensity change.

Dots are separated by using our methodology. First, the optimal threshold values of five different images are computed by minimizing the fitness function Equation (39) using the OEO.²³ Here, the pixel counts of two different classes (N_{C_0} and N_{C_1}) are optimized over the sum, to achieve the optimal threshold values. These optimal thresholds are shown in Table 2. Second, these values are used to achieve the segmented outputs displayed in Figure 5. Note that the entire pixel values less than or equal to the threshold (T) are assigned “0” while

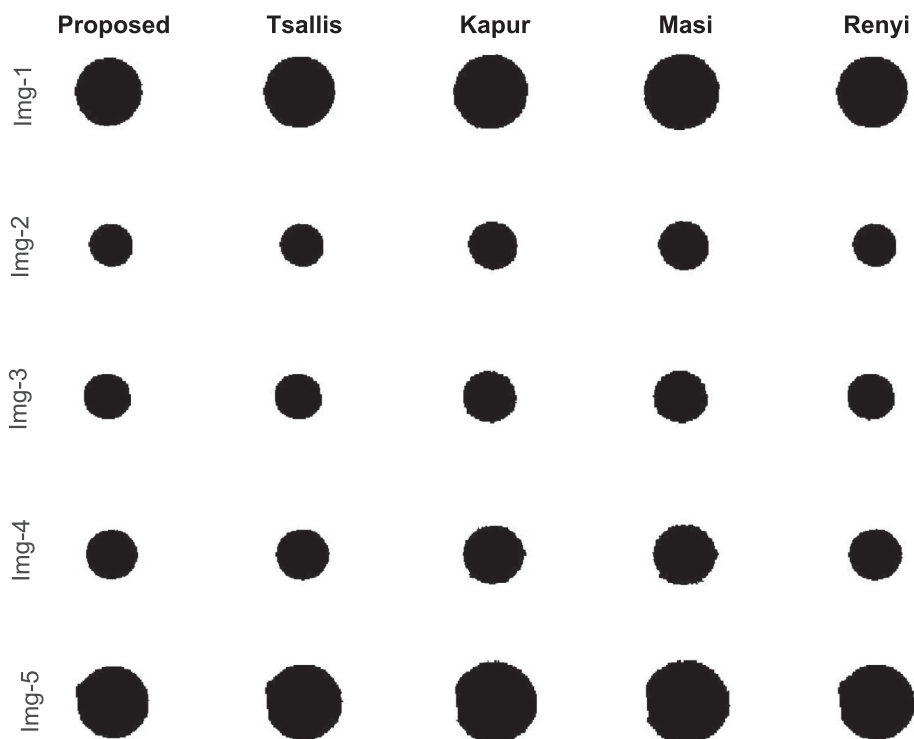


FIGURE 5 Two-class segmented outputs. Dots are separated from the backgrounds.

the other class's pixels are assigned to “255.” For a fair comparison, Tsallis, Kapur's, Masi, and Rényi entropy-based methods for two-class segmentation are also implemented. The parameters for Tsallis, Masi, and Rényi are chosen as 0.1, 0.5, and 0.1 corresponding for the experiments.

In summary, the dots are extracted accurately using our method. This is implicit in Figure 5. From a visual comparison, it is observed that the proposed technique yields better results compared to the Tsallis, Kapur's, Masi, and Rényi entropy-based methods. Especially, the boundaries are exactly located using the suggested method. Other methods fail to detect the intensity change near the boundaries. The reason may be since the entropy-based methods depend on the gray level distribution, because these methods use the image histogram. Particularly in the medical images, the distribution of the gray values is not uniform. On the contrary, our suggested method is efficient, because it does not depend on

the gray level distribution. It optimizes the pixel counts of two different classes adaptively to minimize the segmentation error efficiently.

4.2 | Experiment 2

In this section, the objective function Equation (43) proposed for the multiclass segmentation is used. The idea of minimization of the segmentation error is enlightened in Section 3. The OEO is used for optimization. The optimal threshold values $(T_1^*, T_2^*, \dots, T_K^*)$ are obtained. The output segmented images are constructed using these values. It is reiterated that the output consists of $K + 1$ gray values (classes). The proposal for multiclass segmentation is validated here using 8 numbers of X-Ray chest images displayed in Figure 6. These are randomly chosen from the Kaggle database.^{26–28} An identification number together with its histogram is also displayed.

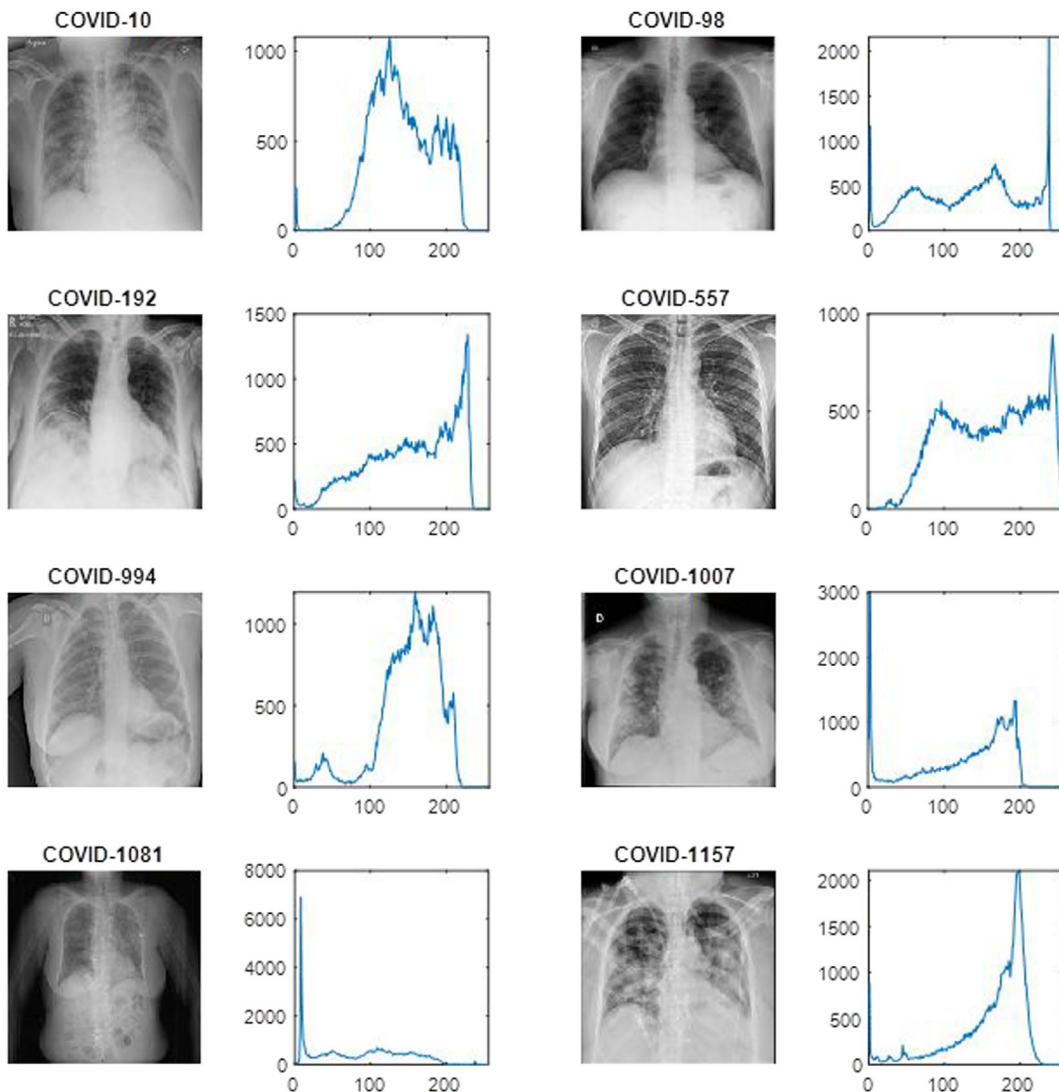


FIGURE 6 Sample X-Ray chest images.

Other objective functions reported by Tsallis, Kapur, Masi, and Rényi are also considered for a fair comparison. The same parameters reported for the OEO in²³ are used here to optimize the objective functions. In this evaluation process, 11 numbers of independent runs are considered for each scheme, to obtain the optimal K numbers of threshold values. Subsequently, these optimal thresholds are used to construct the (output) segmented images. Three different popular metrics are used for an assessment. These are PSNR, FSIM, and SSIM. The higher the values, better the performance. The performance of our method over others is shown in Tables 3–5. The boldface numbers suggest the best results.

From the PSNR values shown in Table 3, it is explicitly clear that our method outperforms other four methods. Similarly, from the FSIM values displayed in Table 4 and the SSIM values shown in Table 5, it is revealed that the proposed technique has dominated the other methods. Additionally, from the quantitative results shown in Table 3, the suggested technique's performance is increased by around 8.03%, while considering the COVID-10 sample image with $K = 2$ with respect to the Tsallis, Kapur, Masi, and Rényi entropy-based schemes. Similarly, it could perform well while considering the data highlighted in Table 4 (FSIM values) and shows an improvement of around 3.01% over other

TABLE 3 Optimal PSNR.

Test image	K	Proposed	Tsallis	Kapur	Masi	Rényi
COVID-10	2	24.1998	22.3145	22.3999	22.3288	22.3322
	3	26.149	25.0937	25.4408	22.2433	25.0502
	4	27.6654	26.5159	27.3422	25.3026	26.576
	5	29.0474	28.0941	28.5516	27.3399	28.0493
COVID-98	2	21.1681	20.5393	20.4982	20.4988	20.5084
	3	23.5277	23.2	23.2588	23.2511	23.218
	4	25.492	25.2949	24.9972	25.0911	25.3125
	5	26.9138	26.9068	26.7594	26.7166	26.9062
COVID-192	2	22.2836	21.4133	21.6922	21.6732	21.4405
	3	24.7076	23.9521	24.3707	24.3842	23.9708
	4	26.5304	25.6415	25.6382	24.4361	25.6861
	5	27.9939	27.3772	26.9816	25.5957	27.2067
COVID-557	2	22.4818	21.3342	22.2558	22.2158	21.392
	3	24.8176	23.5965	22.9097	22.7099	23.6312
	4	26.5985	25.4351	25.3648	25.0999	25.4323
	5	28.0306	27.1036	26.7848	26.847	27.1439
COVID-994	2	24.1912	23.8693	23.9144	19.4999	23.9148
	3	26.918	24.9961	24.9426	23.8098	25.0234
	4	28.5403	26.9289	27.7928	24.8138	26.9289
	5	29.9469	28.1973	28.3243	27.646	28.3221
COVID-1007	2	22.6229	22.4644	21.8805	18.318	22.4476
	3	25.5327	25.1381	24.3499	21.8626	25.2213
	4	27.5213	25.3098	24.4289	24.4348	25.2081
	5	29.2176	27.1965	26.8737	26.513	27.2469
COVID-1081	2	22.6987	21.5394	22.4234	22.4069	21.5025
	3	25.3811	23.0536	22.9196	22.3553	23.0314
	4	27.3286	25.2938	24.8942	24.0839	25.3089
	5	28.8456	27.5067	26.4319	24.7469	27.674
COVID-1157	2	23.5472	23.2614	23.1825	23.1368	23.2388
	3	25.9943	25.6182	25.5581	23.0535	25.5525
	4	27.7447	27.1087	26.7386	25.5395	27.1782
	5	29.331	28.1354	28.1409	27.0823	27.8808

TABLE 4 Optimal FSIM.

Test image	K	Proposed	Tsallis	Kapur	Masi	Rényi
COVID-10	2	0.7273	0.7183	0.7183	0.7083	0.7187
	3	0.7393	0.7419	0.7352	0.707	0.7414
	4	0.7595	0.7346	0.7474	0.7266	0.7361
	5	0.7682	0.7552	0.7626	0.7391	0.753
COVID-98	2	0.6326	0.6561	0.6642	0.6375	0.6548
	3	0.6607	0.6636	0.674	0.6536	0.6644
	4	0.6808	0.6912	0.6955	0.6852	0.69
	5	0.719	0.7185	0.7283	0.7286	0.7203
COVID-192	2	0.6729	0.6854	0.6906	0.6746	0.6848
	3	0.6969	0.6971	0.704	0.6965	0.697
	4	0.7163	0.7166	0.7161	0.6976	0.7171
	5	0.7588	0.7292	0.7383	0.7211	0.7338
COVID-557	2	0.6269	0.6074	0.6349	0.6387	0.6094
	3	0.7087	0.6606	0.6486	0.644	0.6638
	4	0.7588	0.718	0.7171	0.7158	0.7195
	5	0.805	0.7646	0.7641	0.7664	0.765
COVID-994	2	0.7242	0.7442	0.7301	0.7052	0.7454
	3	0.753	0.7345	0.7397	0.7179	0.7347
	4	0.7888	0.7448	0.7574	0.7317	0.7448
	5	0.8174	0.7531	0.7612	0.7569	0.7562
COVID-1007	2	0.6855	0.6986	0.7094	0.6711	0.699
	3	0.7137	0.7168	0.7264	0.6933	0.7183
	4	0.7439	0.7189	0.7246	0.7182	0.7189
	5	0.7731	0.7479	0.7478	0.7521	0.7443
COVID-1081	2	0.7001	0.6986	0.7078	0.6962	0.699
	3	0.7236	0.7084	0.7104	0.6956	0.7082
	4	0.737	0.7146	0.7159	0.6939	0.7142
	5	0.7663	0.7354	0.7297	0.7019	0.738
COVID-1157	2	0.6466	0.6521	0.6562	0.6472	0.6536
	3	0.7013	0.6907	0.6996	0.6457	0.689
	4	0.7457	0.7171	0.7248	0.698	0.7187
	5	0.7907	0.7554	0.7693	0.7374	0.7525

schemes. In case of the optimal SSIM values reported in Table 5, one can observe that our methodology dominates the other schemes and reflects an improvement of around 4.16%. The reason of such improvements may be its inherent mechanism of reducing the segmentation error. Furthermore, its performance is free from the distribution of the gray values. Precisely, our technique is histogram independent.

To further strengthen our results, the entropy values of the thresholded images (output segmented images) are also presented in Table 6. It reveals that, in 81% cases, the proposed scheme yields better entropy values than

the other entropy-based methods. Interestingly, it is seen that, around 9.59% improvement is achieved over Tsallis entropy-based technique while 9.40% improvement over Kapur, 18.61% improvement over Masi, and 9.63% improvement over Rényi entropy-based methods.

For further study, the output segmented images are also presented in Figures 7–10. The segmented outputs for the sample test image COVID-10 and COVID-98 with $K = 2$ are shown in Figure 7. The results for the sample test image COVID-192 and COVID-557 with $K = 3$ is displayed in Figure 8. For the sample test images COVID-994 and COVID-1007 with $K = 4$, the multiclass

TABLE 5 Optimal SSIM.

Test image	K	Proposed	Tsallis	Kapur	Masi	Rényi
COVID-10	2	0.7228	0.7289	0.7278	0.7059	0.7285
	3	0.7446	0.7438	0.7395	0.7011	0.7432
	4	0.7724	0.7456	0.7556	0.7237	0.7474
	5	0.7748	0.7657	0.7732	0.7407	0.7625
COVID-98	2	0.6269	0.6393	0.6471	0.6297	0.6382
	3	0.6631	0.6651	0.6721	0.6583	0.6651
	4	0.6914	0.6982	0.7025	0.6967	0.6977
	5	0.7242	0.7242	0.7324	0.7347	0.7261
COVID-192	2	0.6777	0.6908	0.696	0.6787	0.6895
	3	0.718	0.7209	0.7263	0.7173	0.7216
	4	0.739	0.7424	0.7423	0.7175	0.7427
	5	0.7731	0.7589	0.7664	0.7418	0.7616
COVID-557	2	0.6438	0.6338	0.658	0.6599	0.636
	3	0.7224	0.6775	0.6687	0.6618	0.6803
	4	0.764	0.7318	0.7341	0.7311	0.7341
	5	0.7988	0.7683	0.7658	0.7671	0.767
COVID-994	2	0.7295	0.7545	0.7405	0.7073	0.756
	3	0.7636	0.7464	0.7535	0.7161	0.7474
	4	0.7963	0.7593	0.7727	0.7341	0.7593
	5	0.8168	0.7699	0.777	0.7629	0.7739
COVID-1007	2	0.6514	0.6562	0.6615	0.6099	0.6561
	3	0.7027	0.6842	0.6872	0.6467	0.6882
	4	0.7375	0.6993	0.6826	0.6794	0.7008
	5	0.7676	0.7379	0.722	0.7184	0.7323
COVID-1081	2	0.6282	0.6147	0.6353	0.6171	0.6155
	3	0.7143	0.6394	0.6397	0.6147	0.6388
	4	0.7344	0.6711	0.6572	0.6242	0.6702
	5	0.7662	0.7214	0.6854	0.6371	0.7314
COVID-1157	2	0.6897	0.6934	0.6992	0.6909	0.695
	3	0.7361	0.7286	0.74	0.6891	0.7257
	4	0.77	0.7499	0.7597	0.7338	0.7517
	5	0.8059	0.7655	0.7898	0.7601	0.7615

segmented images are shown in Figure 9. Similarly, the outputs for the sample test images COVID-1081 and COVID-1157 with threshold level $K = 5$ are presented in Figure 10. It is noteworthy to mention here that some important results are presented in this paper, to conserve space. However, all results are analyzed. The results are quite encouraging with quality multiclass segmented outputs. For a fair comparison, it is pertinent to mention here that the label map images are constructed in this experiment.

An in-depth analysis is made to justify the use of the proposed method for COVID-19 chest X-ray image

analysis. It is important to mention here that the gray-level distribution in spatial domain is nonuniform. This is implicit in Figure 6. It is reiterated that the entropy-based methods are dependent on the gray-level distribution. Therefore, the entropy-based methods yield less accurate results. On the contrary, the suggested technique is free from the spatial distribution of gray values. Hence, performs well in this situation. For instance, the multiclass segmented output of the COVID-1157 X-ray image with $K = 5$ proves its effectiveness. In this figure, the class separation is better in our case. The reason of the improvement is mainly due to its sensitivity toward

TABLE 6 Entropy of thresholded image.

Test image	Th	Proposed	Tsallis	Kapur	Masi	Rényi
COVID-10	2	1.6096	1.1664	1.1904	1.1675	1.1766
	3	1.9920	1.6578	1.7411	1.1187	1.6544
	4	2.2396	1.9077	2.0875	1.6985	1.9162
	5	2.3916	2.1657	2.3038	2.0677	2.1636
COVID-98	2	1.5924	1.6132	1.6039	1.6033	1.6117
	3	1.9981	1.9933	2.0188	2.0209	1.9980
	4	2.3204	2.2852	2.2908	2.3000	2.2808
	5	2.5566	2.5431	2.5631	2.5509	2.5433
COVID-192	2	1.5772	1.4228	1.4633	1.4579	1.4254
	3	1.9500	1.8138	1.8716	1.8705	1.8162
	4	2.3062	2.0907	2.0915	1.8576	2.1034
	5	2.5619	2.3840	2.3088	2.0675	2.3524
COVID-557	2	1.6224	1.4971	1.5981	1.5903	1.5042
	3	2.0319	1.8261	1.7051	1.6637	1.8330
	4	2.3446	2.1172	2.1021	2.0643	2.1188
	5	2.6052	2.3951	2.3463	2.3576	2.4100
COVID-994	2	1.3652	1.2916	1.4108	0.4411	1.2960
	3	1.8810	1.5154	1.5006	1.3377	1.5217
	4	2.2458	1.8814	2.0029	1.4239	1.8814
	5	2.5151	2.0691	2.0863	1.9317	2.0769
COVID-1007	2	1.4730	1.5379	1.5160	0.9589	1.5391
	3	1.9006	1.9563	1.9233	1.4865	1.9521
	4	2.2467	1.8778	1.8874	1.8797	1.8424
	5	2.5497	2.1357	2.1499	2.1500	2.1590
COVID-1081	2	1.5992	1.4559	1.5700	1.5669	1.4474
	3	2.0253	1.6601	1.6302	1.5363	1.6541
	4	2.3359	2.0231	1.9978	1.8980	2.0300
	5	2.5668	2.3255	2.2649	1.9859	2.3286
COVID-1157	2	1.2916	1.1357	1.1296	1.1199	1.1267
	3	1.7166	1.5516	1.5140	1.0760	1.5549
	4	1.9952	1.8923	1.6926	1.4906	1.8860
	5	2.2856	2.2022	1.9506	1.7271	2.1611

the intensity variations. The Average CPU time (in sec.) comparison for one independent run is displayed in Table 7.

From Table 7, it is seen that the computation time is reduced significantly as compared to the exhaustive search results shown in Table 1. The reason is that the optimizer OEO is used here. Further, it is observed from Table 7 that, the suggested method needs more time compared to other entropy-based methods. The reason may be due to the adjustment of the pixel counts by changing the class weights iteratively. This may be the disadvantage of the proposed method. However, it shows better

performances in terms of PSNR, SSIM, FSIM, entropy values etc. displayed in Tables 3–6.

4.3 | Novelty of the proposed framework and compliance

The novelty of the developed methodology is its ability to adaptively adjust the class weights. To be specific, these class weights are iteratively adjusted so that the segmentation error gets minimized. The patient image data can be divided into two or more segments. It would be useful

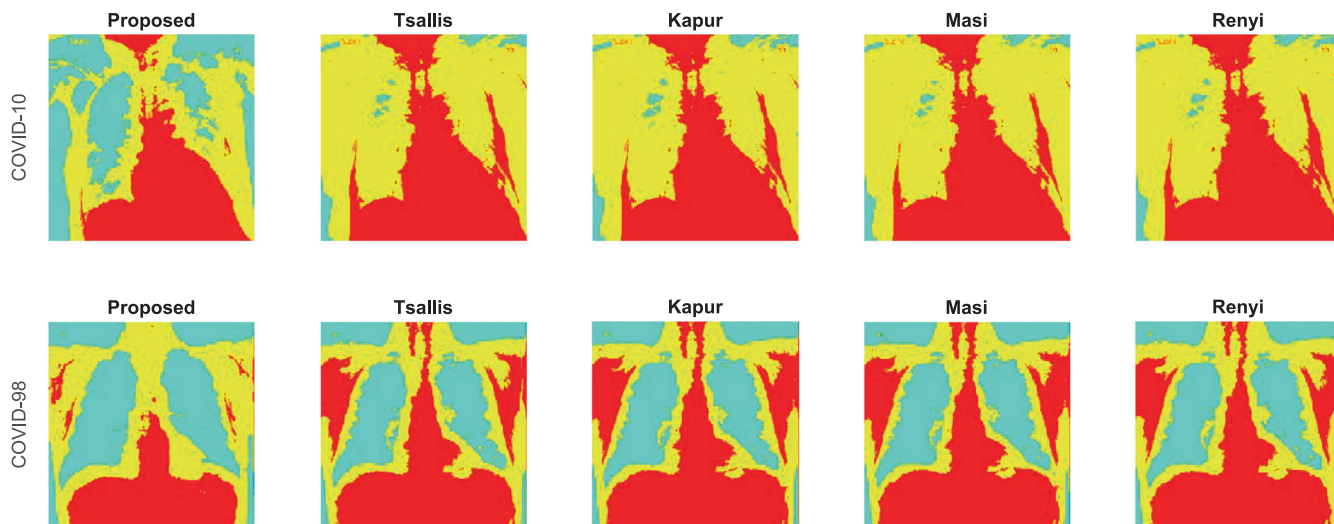


FIGURE 7 Results with Sample test images COVID-10 and COVID-98 with threshold level $K = 2$.

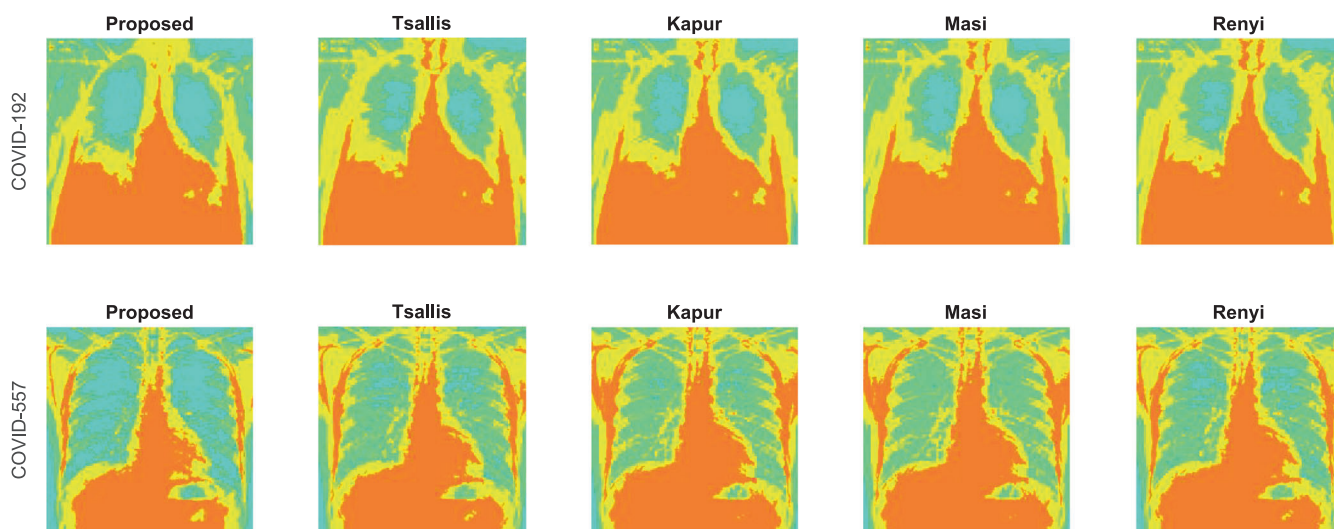


FIGURE 8 Results with Sample test images COVID-192 and COVID-557 with threshold level $K = 3$.

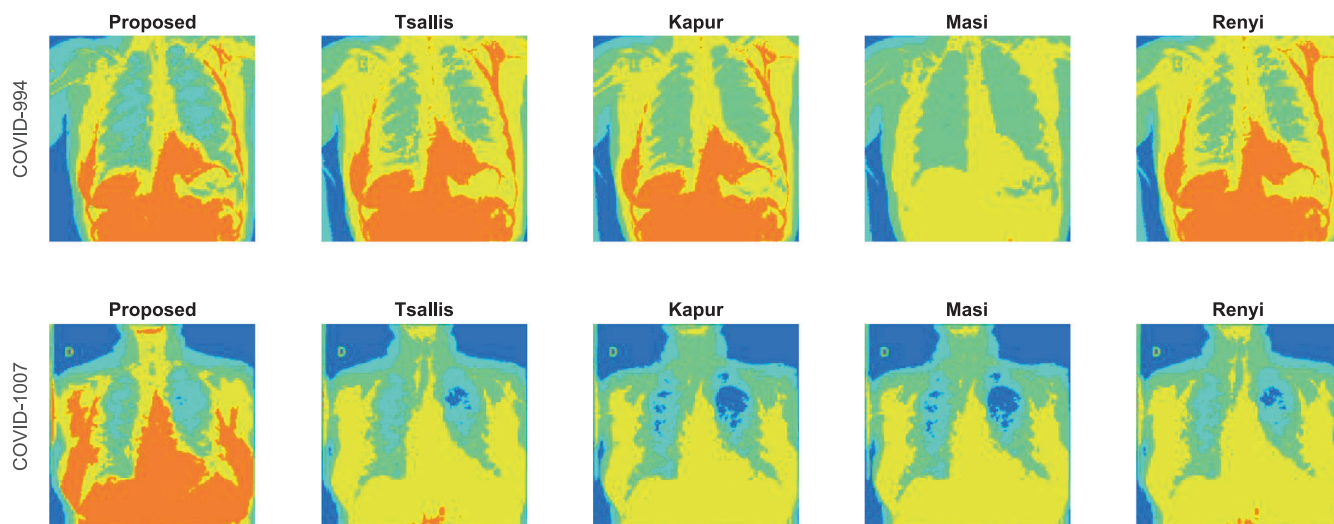


FIGURE 9 Results with Sample test images COVID-994 and COVID-1007 with threshold level $K = 4$.

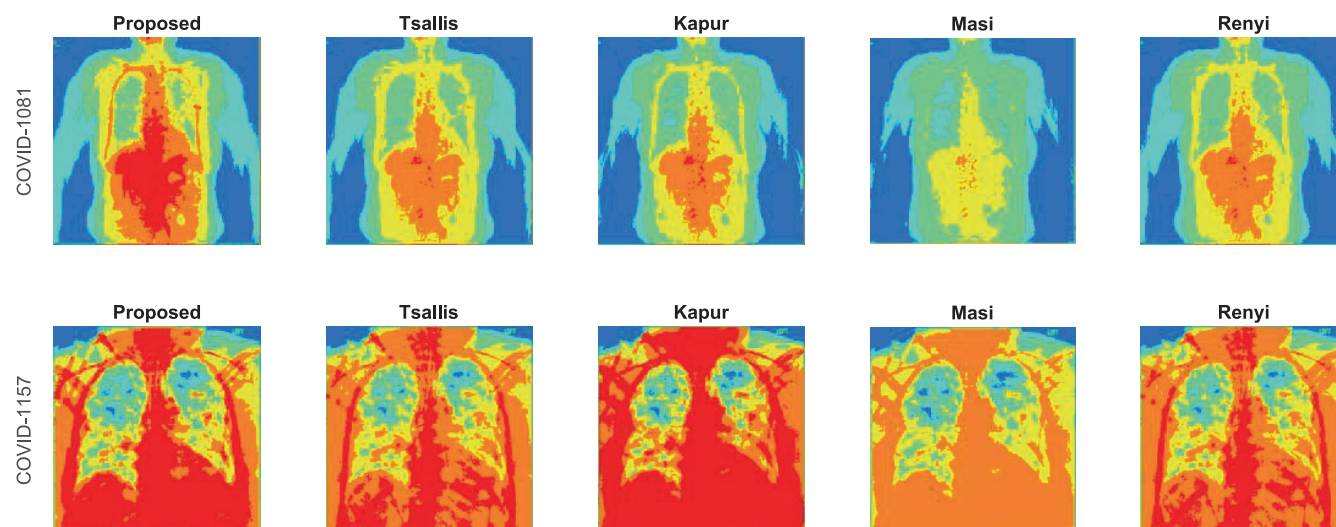


FIGURE 10 Results with sample test images COVID-1081 and COVID-1157 with threshold level $K = 5$.

TABLE 7 Average CPU time (in sec.) comparison for one independent run using the OEO.

Th	Proposed	Tsallis	Kapur	Masi	Rényi
2	2.1311	1.5789	1.9577	1.5506	1.5456
3	2.6729	1.6869	1.9891	1.5936	1.6915
4	3.3667	1.7742	2.0033	1.6214	1.7190
5	3.8072	1.8763	2.0466	1.6528	1.7421

to the medical profession for analyzing the medical images such as micro-array dots and chest X-ray images. While developing the platform, we have also done our best to comply with the Health Insurance Portability and Accountability Act (HIPAA) standardizing best practices for maintaining the security and privacy of healthcare data. We have emphasized the need for implementation and documentation of administrative, physical, and technical safeguards for the software platform handling patient health information. This project is in the beta phase and once it is decided to adopt in a real environment, we plan to add more security layers to prevent cyberattacks and unauthorized access.

5 | CONCLUSION

The paper suggested a novel adaptive class weight adjustment-based multiclass segmentation error minimization method for analysis of the chest COVID-19 X-ray images. The technique used mean intensity values in a class. The novelty of the idea is that the mean value is unbiased of the spatial distribution. The proposal is very simple to implement and is the fastest of all the


methods based on the entropy computation using the image histogram. It is also found better than others, because it is not affected due to the nonuniform distribution of the gray levels in the image histogram. It yields better values, because the inherent mechanism is quite effective to reduce the segmentation error. It has a better sense of handling the intensity variation. The opposition equilibrium optimizer is used for minimizing the fitness values. The suggested methodology may be the best option for the multiclass segmentation of biomedical images. The technique yields quality segmented images for the COVID-19 X-ray images, due to the minimization of the segmentation error. There are certain merits in the proposed scheme. To figure out – (i) better segmentation results, (ii) faster convergence, and (iii) does not depend on the distribution of the gray level values. It means, convincingly, this scheme would be very useful for the analysis of the COVID-19 chest X-ray images. It is believed that the two-class segmentation idea would be well-suited for extracting the dots from the DNA sequence images. It may also be used for the document image analysis. Interestingly, this work may also stretch a new direction to the multiclass segmentation of the medical images. There is enough scope for extending the idea for multiclass segmentation of the color images, brain MR images, and breast cancer thermograms.

DATA AVAILABILITY STATEMENT

The data that support the findings of this study are available in COVID-19 Radiography Database | Kaggle at <https://www.kaggle.com/tawsifurrahman/covid19>, reference number.²⁸ These data were derived from the following resources available in the public domain: – COVID-19

Radiography Database | Kaggle, <https://www.kaggle.com/tawsifurrahman/covid19>.

ORCID

Rutuparna Panda  <https://orcid.org/0000-0002-8676-0144>

REFERENCES

1. Taleghani N, Taghipour F. Diagnosis of COVID-19 for controlling the pandemic: a review of the state-of-the-art. *Biosens Bioelectron.* 2021;174:112830.
2. Feng H, Liu Y, Lv M, Zhong J. A case report of COVID-19 with false negative RT-PCR test: necessity of chest CT. *Jpn J Radiol.* 2020;38(5):409-410.
3. Yasin R, Gouda W. Chest X-ray findings monitoring COVID-19 disease course and severity. *Egypt J Radiol Nucl Med.* 2020; 51:193.
4. Liu L, Zhao D, Yu F, et al. Ant colony optimization with Cauchy and greedy levy mutations for multilevel COVID 19 X-ray image segmentation. *Comput Biol Med.* 2021;136:104609.
5. Abdel-Basset M, Chang V, Mohamed R. HSMA_WOA: a hybrid novel slime mould algorithm with whale optimization algorithm for tackling the image segmentation problem of chest X-ray images. *Appl Soft Comput.* 2020;95:106642.
6. Sharma A, Chaturvedi R, Kumar S, Dwivedi UK. Multi-level image thresholding based on Kapur and Tsallis entropy using firefly algorithm. *J Interdiscip Math.* 2020;23(2):563-571.
7. Su H, Zhao D, Elmannai H, et al. Multilevel threshold image segmentation for COVID-19 chest radiography: a framework using horizontal and vertical multiverse optimization. *Comput Biol Med.* 2022;105618:105618.
8. Murillo-Olmos J et al. Thresholding algorithm applied to chest X-ray images with pneumonia. In: Oliva D, Houssein EH, Hinojosa S, eds. *BT – Metaheuristics in Machine Learning: Theory and Applications*. Springer International Publishing; 2021: 359-407.
9. Chakraborty S, Saha AK, Nama S, Debnath S. COVID-19 X-ray image segmentation by modified whale optimization algorithm with population reduction. *Comput Biol Med.* 2021;139:104984.
10. Ayala HVH, dos Santos FM, Mariani VC, dos Coelho L. Image thresholding segmentation based on a novel beta differential evolution approach. *Expert Syst Appl.* 2015;42(4):2136-2142.
11. Masi M. A step beyond Tsallis and Rényi entropies. *Phys Lett Sect A Gen At Solid State Phys.* 2005;338(3-5):217-224.
12. Wunna A, Kumar Naik M, Panda R, Jena B, Abraham A. A differential evolutionary adaptive Harris hawks optimization for two dimensional practical Masi entropy-based multilevel image thresholding. *J King Saud Univ Comput Inform Sci.* 2020;34(6):3011-3024. doi:10.1016/j.jksuci.2020.05.001
13. Wei L, Huang Y, Ye Z, et al. Rényi's entropy based multilevel thresholding using a novel meta-heuristics algorithm. *Appl Sci.* 2020;10(9):3225.
14. Zaitoun NM, Aqel MJ. Survey on Image Segmentation Techniques. *Procedia Comput Sci.* 2015;65:797-806.
15. Agrawal S, Panda R, Bhuyan S, Panigrahi BK. Tsallis entropy based optimal multilevel thresholding using cuckoo search algorithm. *Swarm Evol Comput.* 2013;11:16-30.
16. Khairuzzaman AKM, Chaudhury S. Multilevel thresholding using grey wolf optimizer for image segmentation. *Expert Syst Appl.* 2017;86:64-76.
17. Baby Resma KP, Nair MS. Multilevel thresholding for image segmentation using krill herd optimization algorithm. *J King Saud Univ Comput Inform Sci.* 2018;33(3):1-14.
18. El Aziz MA, Ewees AA, Hassanien AE. Whale optimization algorithm and moth-flame optimization for multilevel thresholding image segmentation. *Expert Syst Appl.* 2017;83:242-256.
19. He L, Huang S. Modified firefly algorithm based multilevel thresholding for color image segmentation. *Neurocomputing.* 2017;240:152-174.
20. Sarkar S, Das S. Multilevel image Thresholding based on 2D histogram and maximum Tsallis entropy— a differential evolution approach. *IEEE Trans Image Process.* 2013;22(12):4788-4797.
21. Sarkar S, Das S, Chaudhuri SS. Hyper-spectral image segmentation using Rényi entropy based multi-level thresholding aided with differential evolution. *Expert Syst Appl.* 2016;50: 120-129.
22. Faramarzi A, Heidarinejad M, Stephens B, Mirjalili S. Equilibrium optimizer: a novel optimization algorithm. *Knowledge-Based Syst.* 2020;191:105190.
23. Naik MK, Panda R, Abraham A. An opposition equilibrium optimizer for context-sensitive entropy dependency based multilevel thresholding of remote sensing images. *Swarm Evol Comput.* 2021;65:100907.
24. Qin D. Next-generation sequencing and its clinical application. *Cancer Biol Med.* 2019;16:1. <http://www.cbiportal.org/2Fj.issn.2095-3941.2018.0055>
25. <http://www.cbiportal.org/>
26. Rahman T, Khandakar A, Qiblawey Y, et al. Exploring the effect of image enhancement techniques on COVID-19 detection using chest X-ray images. *Comput Biol Med.* 2021;132: 104319.
27. Chowdhury MEH, Rahman T, Khandakar A, et al. Can AI help in screening viral and COVID-19 pneumonia? *IEEE Access.* 2020;8:132665-132676.
28. COVID-19 Radiography Database | Kaggle. 2022 <https://www.kaggle.com/tawsifurrahman/covid19-radiography-database>
29. Sanghvi HA, Patel RH, Agarwal A, Gupta S, Sawhney V, Pandya AS. A deep learning approach for classification of COVID and pneumonia using DenseNet-201. *Int J Imaging Syst Technol.* 2023;33(1):18-38.
30. Parmar V, Sanghvi HA, Patel RH, Pandya AS. A Comprehensive Study on Password Less Authentication. In 2022 International Conference on Sustainable Computing and Data Communication Systems (ICSCDS), 2022, 1266-1275.

How to cite this article: Samantaray L, Panda R, Naik MK, Abraham A. A novel adaptive class weight adjustment-based multiclass segmentation error minimization technique for COVID-19 X-ray image analysis. *Int J Imaging Syst Technol.* 2023; 1-17. doi:10.1002/ima.22916